Supplemental Information for

Precise Control of Process Parameters for >23% Efficiency Perovskite Solar Cells in Ambient Air Using an Automated Device Acceleration Platform

Jiyun Zhang[1,2]*, Jianchang Wu[1,2], Anastasia Barabash[2], Tian Du[1,2], Shudi Qiu[2], Vincent M. Le Corre[1,2], Yicheng Zhao[3], Kaicheng Zhang[2], Frederik Schmitt[1], Zijian Peng[2], Jingjing Tian[2], Chaohui Li[2], Chao Liu[1,2], Thomas Heumueller[1,2], Larry Lüer[2], Jens A. Hauch[1,2], and Christoph J. Brabec[1,2,4]*

[1]Forschungszentrum Jülich GmbH, Helmholtz-Institute Erlangen-Nürnberg (HI ERN), Department of High Throughput Methods in Photovoltaics, Immerwahrstraße 2, 91058 Erlangen, Germany

[2]Friedrich-Alexander-University Erlangen-Nuremberg (FAU), Faculty of Engineering, Department of Material Science, Institute of Materials for Electronics and Energy Technology (i-MEET), Martensstrasse 7, 91058 Erlangen, Germany

[3]University of Electronic Science and Technology of China (UESTC), State Key Laboratory of Electronic Thin Films and Integrated Devices, School of Electronic Science and Engineering, 611731 Chengdu, China

[4]Lead Contact

*Corresponding: jiyun.zhang@fau.de and christoph.brabec@fau.de

Experimental Section

Raw Chemicals

Lead iodide (PbI_2, 99.999%), lithium bis(trifluoromethanesulfonyl) imide (LiTFSI), anhydrous N, N-dimethylformamide (DMF, 99.8%), dimethyl sulfoxide (DMSO, 99.9%), cesium iodide (CsI, 99.999%), tris(2-(1H-pyrazol-1-yl)-4-tert-butylpyridine)cobalt(III) tri[bis(trifluoromethane)sulfonimide] (FK 209 Co(III) TFSI salt), and chlorobenzene (CB, anhydrous, 99.8%) were purchased from from Sigma Aldrich. The tin(IV) oxide (SnO_2, 15% in H_2O colloidal dispersion) was bought from Alfa Aesar. Formamidinium iodide (FAI, 99.5%), poly[bis(4-phenyl)(2,4,6-trimethylphenyl)amine] (PTAA), 2,2',7,7'-Tetrakis[N,N-di (4-methoxyphenyl)amino]-9,9'-spirobi fluorene (Spiro-OMe TAD, 99.8%), and methylammonium chloride (MACl, 99.9%) were purchased from Xi'an Yuri Solar Co., Ltd. Phenethylammonium iodide (PEAI, 99.5%) was purchased from Greatcell Solar. All reagents were used as received without further purification and additional treatment.

Solution Preparation

The SnO_2 solution was prepared by mixing 300 µL SnO_2 aqueous solution with 1.5 mL mixed solvent of isopropanol (IPA) and deionized water (volume ratio, 1:1). The perovskite composition used in our experiment is represented as $FA_xCs_{1-x}PbI_3$. The PbI_2/CsI precursor solution was obtained by dissolving 1.5 M PbI_2 and CsI (molar ratio of 95:5) in 1 mL of DMSO and DMF mixed solvent (volume ratio of 1:9). The organic ammonium halide solution was prepared by dissolving FAI: MACl (60 mg: 6 mg) in 1 mL IPA. 1 mg/mL PEAI solution was prepared by dissolved PEAI in IPA. 1 mL Spiro-OMeTAD solution was prepared by dissolving 72.3 mg Spiro-OMeTAD in CB, and then adding 17.5 µL LiTFSI (520 mg/mL in methyl cyanide, MeCN), 28.8 µL Co(III) TFSI salt (300 mg/mL in MeCN) and 28.8 µL *4-tert*-butylpyridin (*t*-BP). PDCBT solution was obtained by dissolving PDCBT in chloroform at 15 mg/mL. The PTAA-BCF solution was prepared by dissolving 1 mg tris (pentafluorophenyl) borane (BCF) into 15 mg/mL PTAA solution. All solutions were filtered by polytetrafluoroethylene (PTFE, 0.2 µm) filter before use.

Device Fabrication

1-inch ITO substrates were sonicated in deionized water, acetone, and IPA solvents for 10 min, respectively. The substrates were then dried with compressed air and treated with UV-ozone for 15 min before use. The two-step sequential deposition method was used to fabricate the full perovskite devices in ambient air. The SnO_2 layer was prepared by depositing 65 µL SnO_2 solution onto ITO substrate at 4000 rpm for 60 s through the SPINBOT platform and the substrate was then annealed at 150°C for at least 30 min in ambient air. After cooling down, a wet PbI_2/CsI film was formed onto the SnO_2–coated substrates by dripping 50 µL PbI_2/CsI precursor

through on-the-fly mode at 1300 rpm for 15 s without annealing. When the spin-coater accelerated to 1750 rpm for 30 s at the second stage, 100 μL organic ammonium halide solution was then dripped onto the preformed wet PbI_2 film at 15 s, followed by annealing at 150°C for 15 min in ambient air. Meanwhile, nitrogen gas flow was supplied into the spin-coater to remove the residual solvent vapor. A vacuum pump was applied to accelerate the removal process of residual solvent vapor during and after the deposition process. The final solution-processed deposition involved the formation of Spiro-OMeTAD as hole-transporting layer, which was deposited at 4000 rpm for 45 s through a static mode without thermal annealing. For the devices fabricated with the optimized parameters, a thin PEAI layer was spin-coated onto perovskite layer at 4000 rpm for 30 s, followed by annealing at 100°C for 5 min. All the above solution-processed depositions were performed through the SPINBOT platform in the ambient environment. The semi-devices were then transferred to a separate evaporation chamber manually for electrode deposition. A 60-nm-thick Au layer was finally deposited through a shadow mask (area 0.063 cm^2) *via* thermal evaporation. In the fabrication of devices for phot-thermal stability test, Spiro-OMeTAD was replaced by the PDCBT and BCF-doped PTAA bilayer. The PDCBT layer was formed by spin-coating precursor onto perovskite film at 2000 rpm for 40 s, followed by annealing at 90°C for 5 min. 100 μL PTAA-BCF solution was deposited on the PDCBT layer at 2000 rpm for 30 s through a static mode, without annealing. A 200-nm-thick MgF_2 layer was thermally evaporated onto the device after Au-electrode evaporation with a square mask at a speed of 1Å/s.

Film Characterizations

XRD: Crystallographic information of the thin films was obtained by X-ray diffraction characterization utilizing a Panalytical X'pert powder diffractometer (Cu-K_α radiation, λ = 0.154 nm) and an X'Celerator solid-state stripe detector with conditions of 40 kV and 30 mA.

SEM: The top-view microstructure images were obtained by field emission scanning electron microscope (SEM, HITACHI S4800) using a 10 kV acceleration voltage.

Thickness: The thin film thickness was measured using a Tencor Stylus Profilometers. The stylus force was 0.50 mg and testing speed was 0.1 mm/s.

PL and UV-Vis Absorption Spectra: The high-throughput in-situ characterization for steady-state photoluminescence (PL) and UV-Vis absorption spectra was performed with TECAN infinite 200 Pro in ambient air. The PL signal was gained from the central position of films from 500 nm to 850 nm with a 5 nm scanning step (λ_{ex} = 450 nm). The absorbance spectra were gathered from 600 nm to 900 nm with a 3 nm step size. The PL and absorption data were collected by the Visual Basic for Applications

(VBA) programming. The detailed PL peak position and intensity were obtained through Gaussian fitting based on a Python code. To map the PL intensity distribution of the samples, the contour figures were drawn by positioning the PL intensity values (13 positions) as a function of characteristic positions.

In-situ PL Spectra: In-situ PL spectra were measured using a custom-built confocal setup in the air, which included a 532 nm laser diode, a plano-convex lens positioned above the substrate, a 550 nm long-pass filter, and a fiber-coupled spectrometer (AVANTES, ULS2048XL Sensline series). The distance between the plano-convex lens and the substrate was optimized to maximize the PL intensity of a test film.

Thermal-thermal Stability Testing: The unsealed films aged at 65 °C in a nitrogen-filled chamber under continuous 1-sun metal-halide lamp illumination for 2030 h. The samples were transferred back and forth between the analytical setup and the aging setup. A standard program and calibration process were performed before stability tests to make sure that each sample could be measured at the same spot every time.

Device Characterizations

Current Density–Voltage (*J–V*) Curves: *J-V* curves were characterized using a Keithley source under 100 mW/cm^2 AM 1.5G illumination (Newport Solla simulator). The light intensity was calibrated with a crystalline Si-cell. The *J-V* spectra were obtained from -0.2 to 1.2 V (forward scan) and 1.2 to -0.2 V (reverse scan) at a scan rate of 0.04 V/s. An aperture mask with an area of 0.063 cm^2 was used.

EQE Spectra: The external quantum efficiency (EQE) spectra were recorded on a commercial EQE measurement system (Enlitech, QE-R) under ambient conditions and the light intensity at each wavelength was calibrated with a standard single-crystal Si photovoltaic cell.

MPP Tracking: The steady-state output of the unpacked device with MPP tracking under simulated AM 1.5G illumination in ambient air with continuous nitrogen flow. The data is collected at J_{mpp} with a constant voltage (V_{mpp}) of 0.908 V.

Stability Test: The devices were placed in a home-built degradation chamber with nitrogen flow and continuously illuminated by a metal-halide lamp. The light source was provided by white light-emitting diodes (XLamp CXA2011 1,300 K CCT) and metal-halide lamps with 83 mW/cm^2 intensity, respectively. The temperature (60-65°C) of the chamber was controlled by a hotplate beneath the chamber and was monitored by a thermocouple meter during aging.

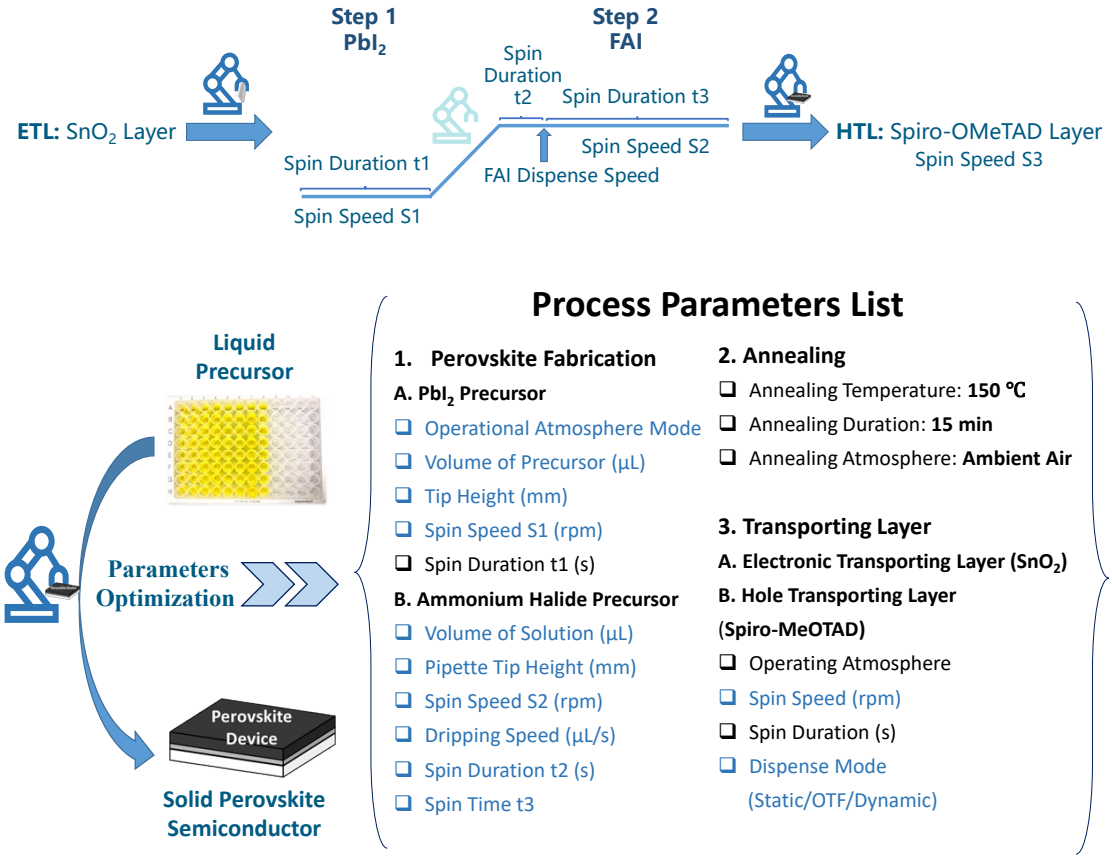

Fig. S1 The procedure and process parameter list involved the automatic fabrication of full metal-halide PSCs with a structure of ITO/SnO_2/Perovskite/Spiro-OMeTAD/Au using a two-step sequential method in the ambient environment. The parameters highlighted in blue were optimized in this study.

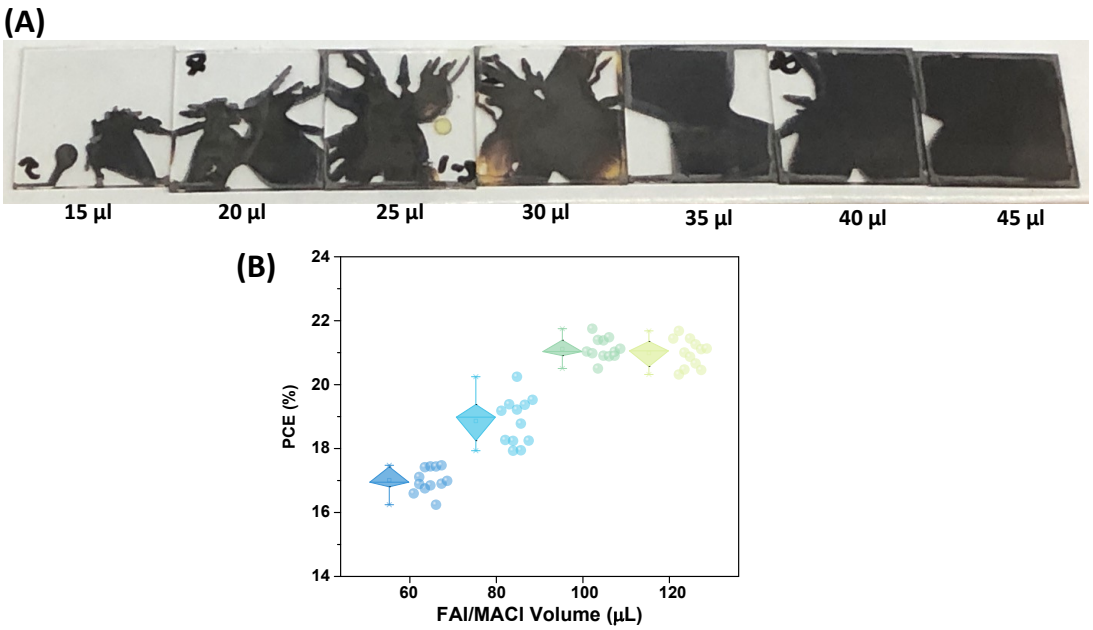

Fig. S2 (A) The photographs of perovskite thin films fabricated with various volumes of PbI_2/CsI precursor. The precursors were deposited onto SnO_2-coated common substrates. **(B)** Performance distribution of perovskite devices fabricated with various volumes of FAI/MACl solution. The volumes are 60, 80, 100, and 120 µL, respectively. (Spin speed combination: 1300 rpm * 1750 rpm)

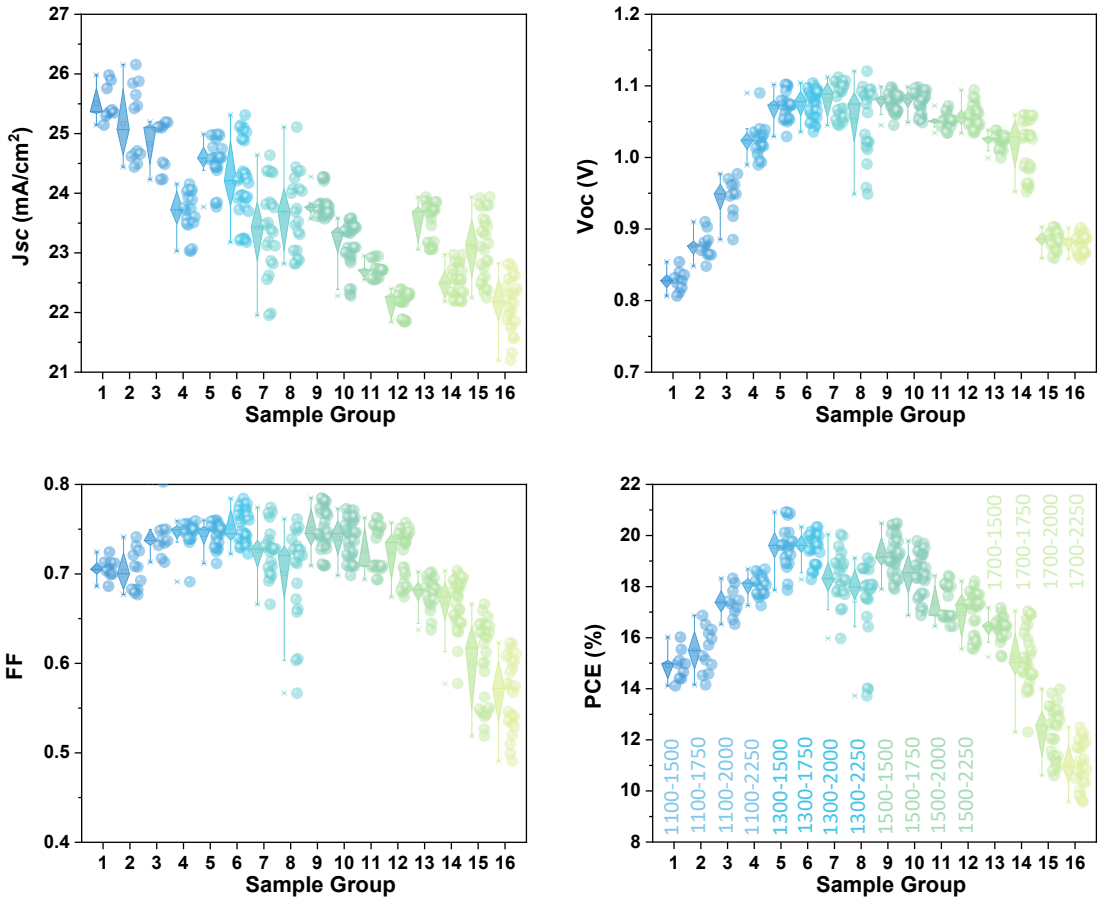

Fig. S3 Grouped performance distribution of perovskite solar devices with various spin speed combinations for the combined PbI_2/CsI and ammonium salt layer. Insert text gives the detailed parameter information.

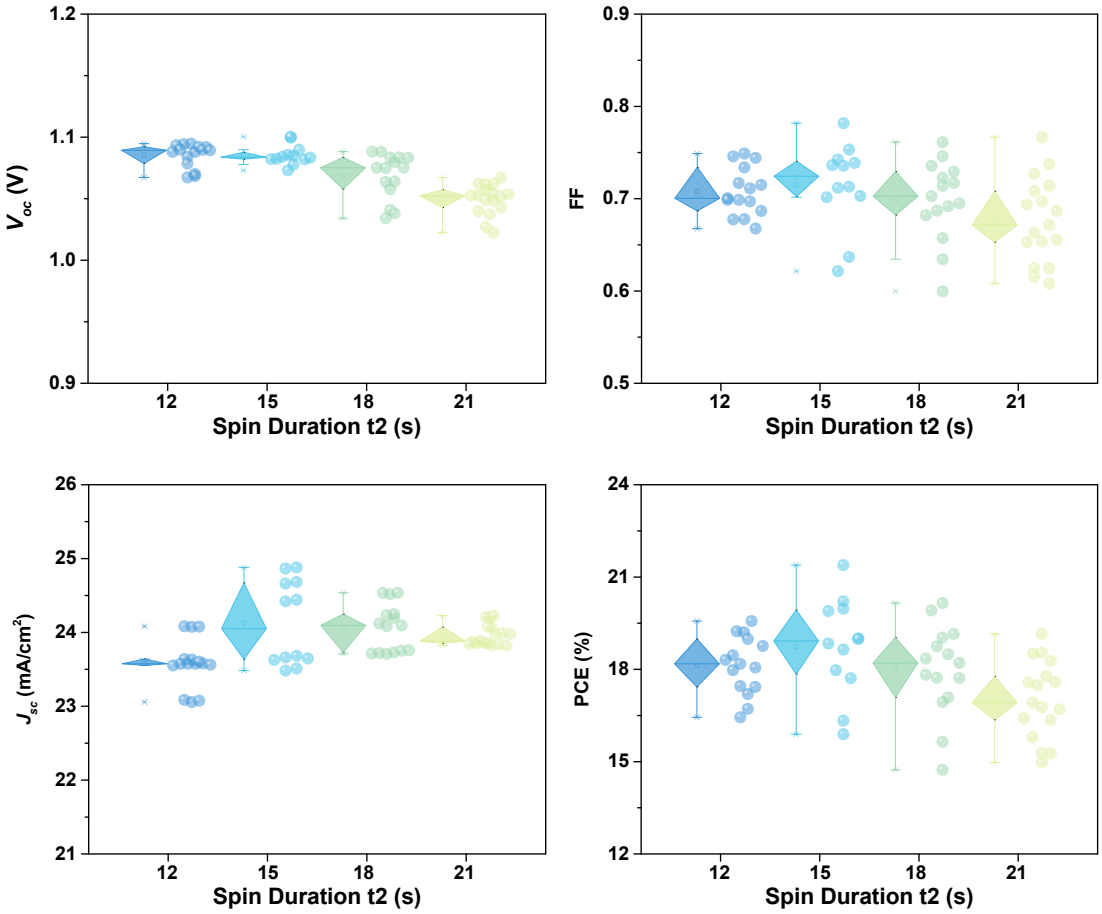

Fig. S4 Grouped performance statistics of perovskite devices fabricated with varying spin durations (t2). The durations are 12, 15, 18, and 21 s, respectively.

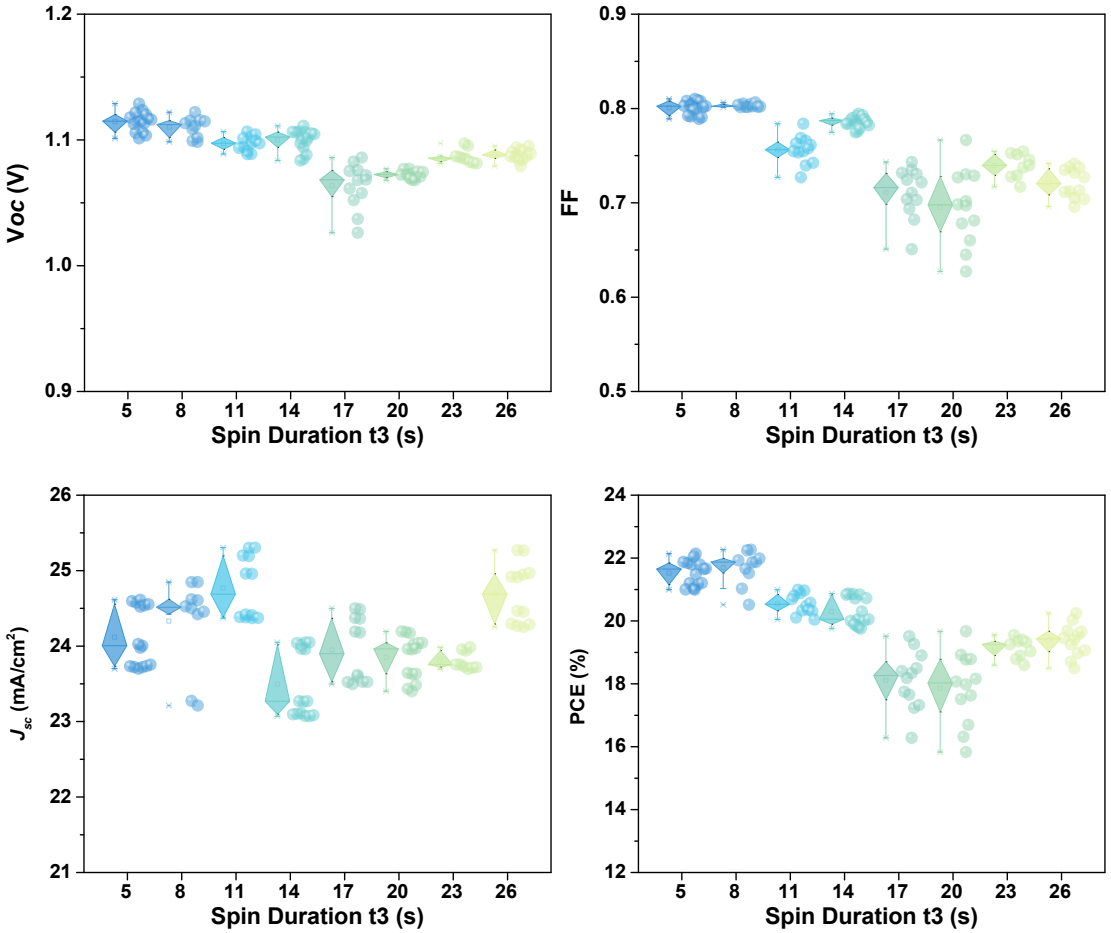

Fig. S5 Grouped performance statistics for perovskite devices fabricated with different spin durations (t3) after FAI/MACl dripping. The spin durations are 5, 8, 11, 14, 17, 20, 23, and 26 s, respectively.

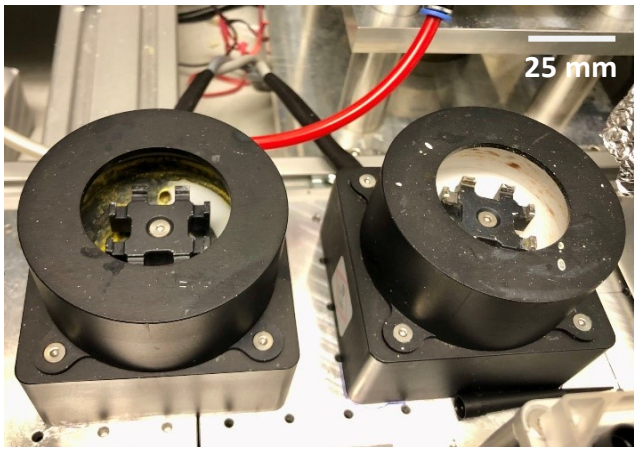

Fig. S6 The mini spin-coaters of the SPINBOT platform.

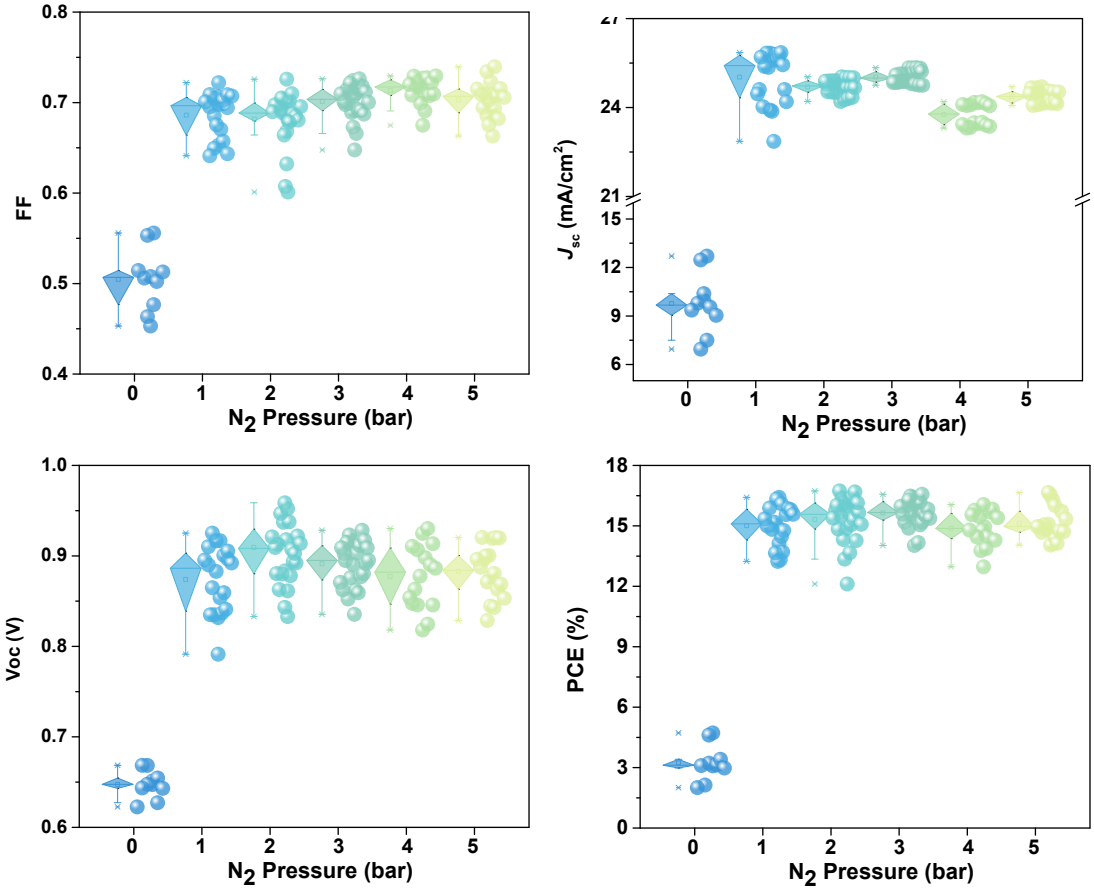

Fig. S7 Grouped performance statistics for perovskite devices fabricated under various operational atmospheres. The gas pressures are 0, 1, 2, 3, 4, and 5 bar, respectively.

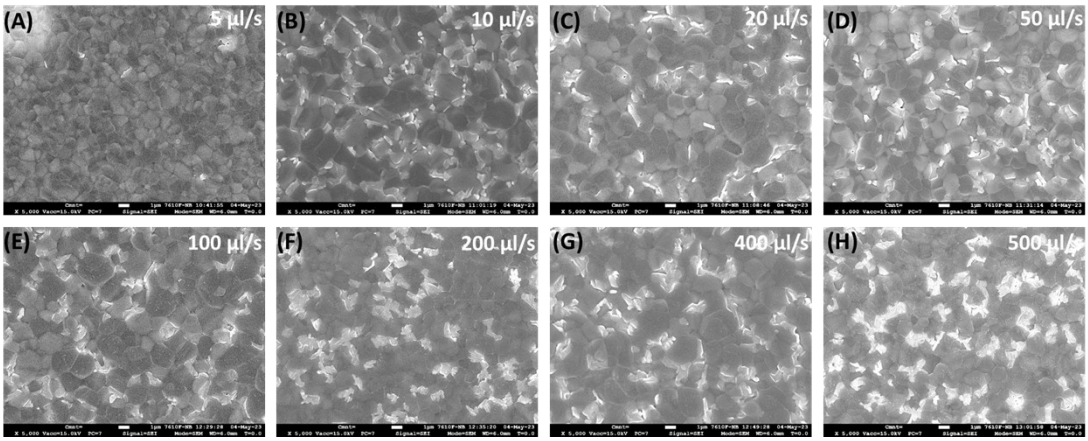

Fig. S8 Top-view SEM images of perovskite films produced with different dripping speeds of organic ammonium halide precursor. **(A-H)** The speeds are 5, 10, 20, 50, 100, 200, 400, and 500 µL/s, respectively. The scale bar is 1 µm.

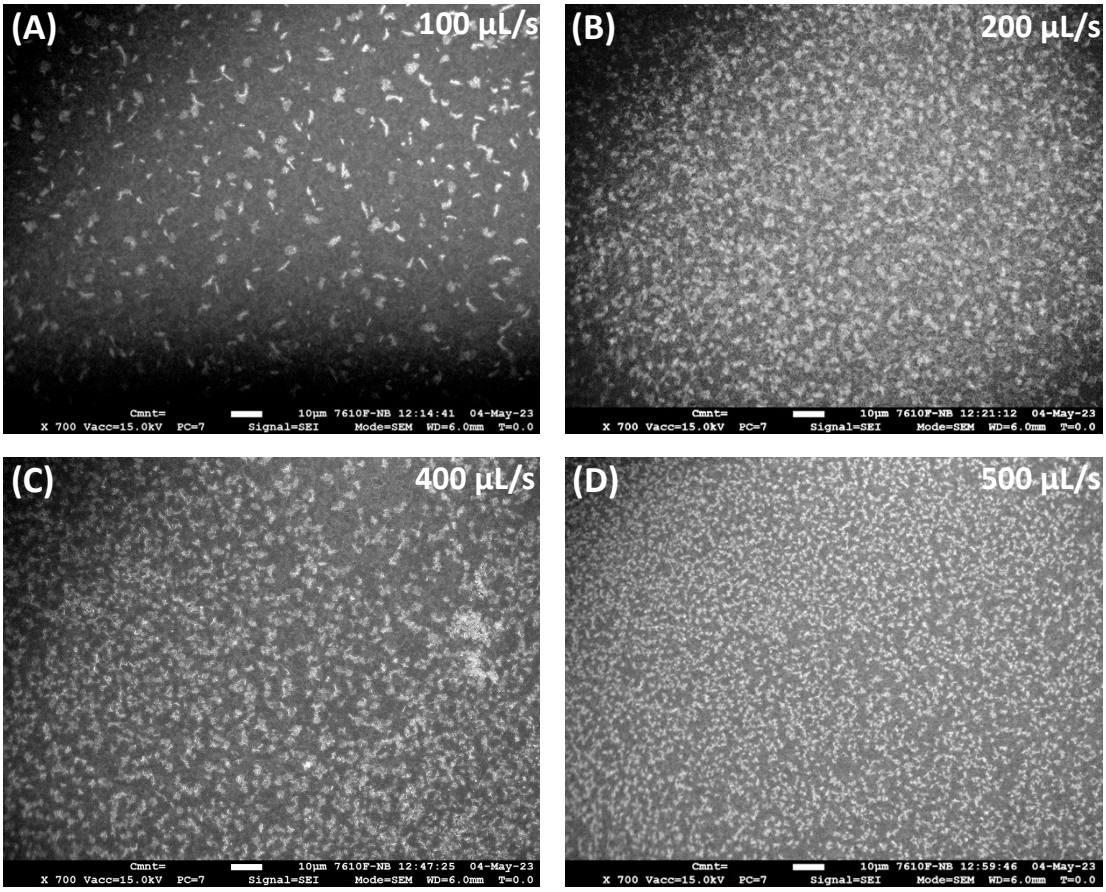

Fig. S9 Top-view SEM images of perovskite films prepared with different dripping speeds of organic ammonium halide precursor. **(A-D)** The speeds are 100, 200, 400, and 500 µL/s, respectively. The scale bar is 10 µm.

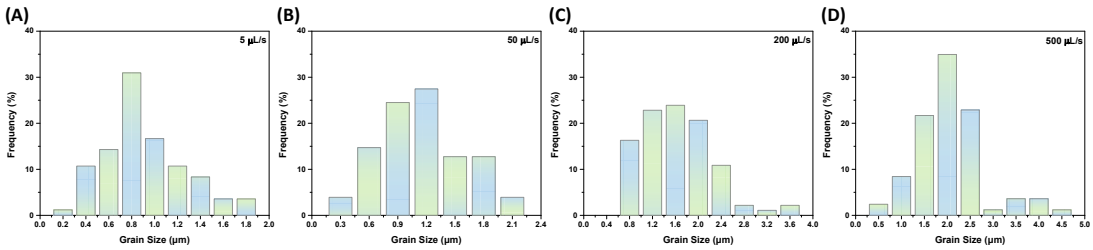

Fig. S10 The grain size distribution of perovskite thin films produced with varying dripping speeds of ammonium halide solution. The dripping speeds are **(A).** 5, **(B).** 50, **(C).** 200, and **(D).** 500 µL/s, respectively.

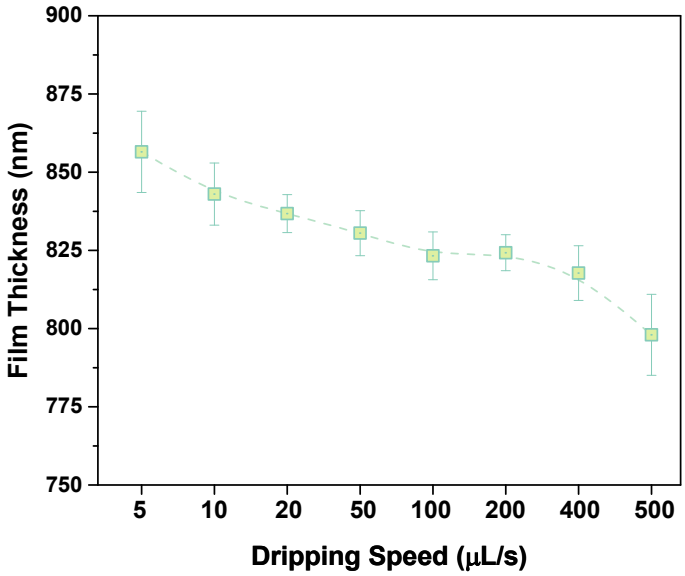

Fig. S11 The thickness of perovskite films fabricated with different dripping speeds of organic ammonium halide precursor. The samples were produced through the automated platform. The dripping speeds are 5 to 500 μL/s.

Fig. S12 Photographs of perovskite thin films produced with different dripping speeds of organic ammonium halide solution. The ejection speeds are 0.5, 1, 2, 4, 5, 10, 20, 50, 100, 200, 400, and 500 μL/s, respectively.

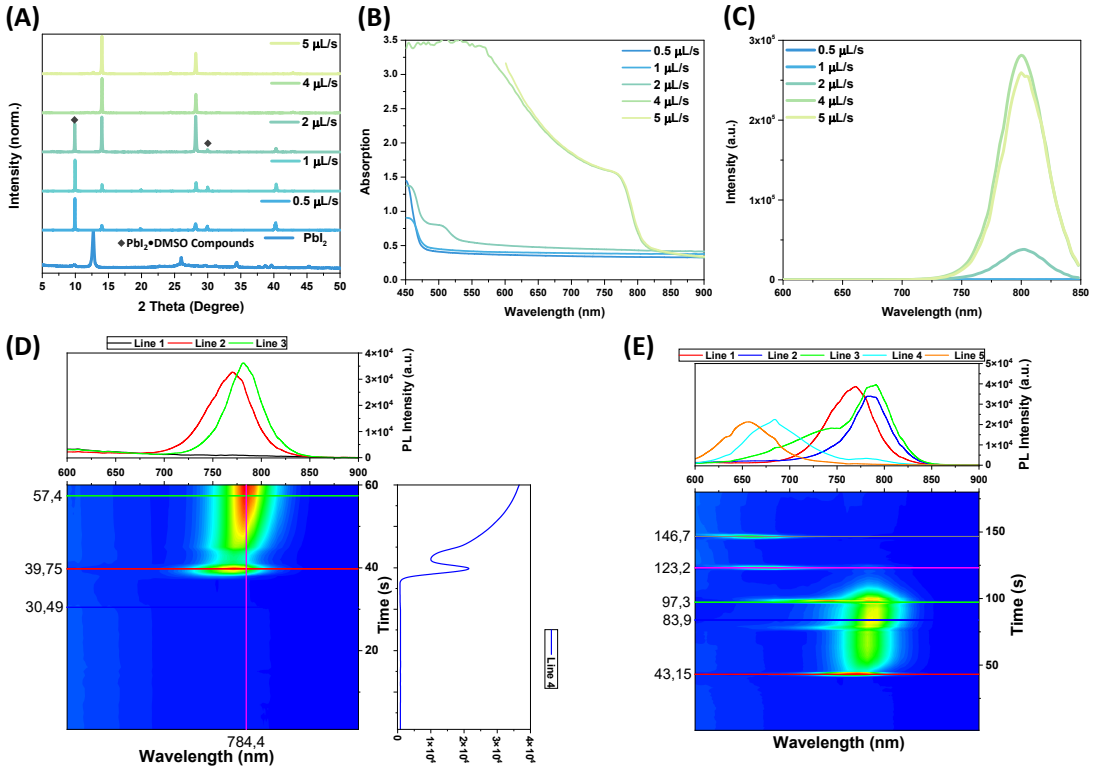

Fig. S13 (A) XRD patterns, **(B)** UV-Vis absorption spectra and **(C)** PL spectra of perovskite films fabricated with different dripping speeds of organic ammonium halide precursor. The samples were produced through the automated platform. The dripping speeds are 0.5, 1, 2, 4, and 5 µL/s, respectively. In-situ PL spectra of perovskite films with **(D)** fast (>50 µL/s) and **(E)** very slow (<0.5 µL/s) ejection speeds of FAI/MACl. The samples are fabricated manually. Spin speed combination: 1300 rpm * 1750 rpm.

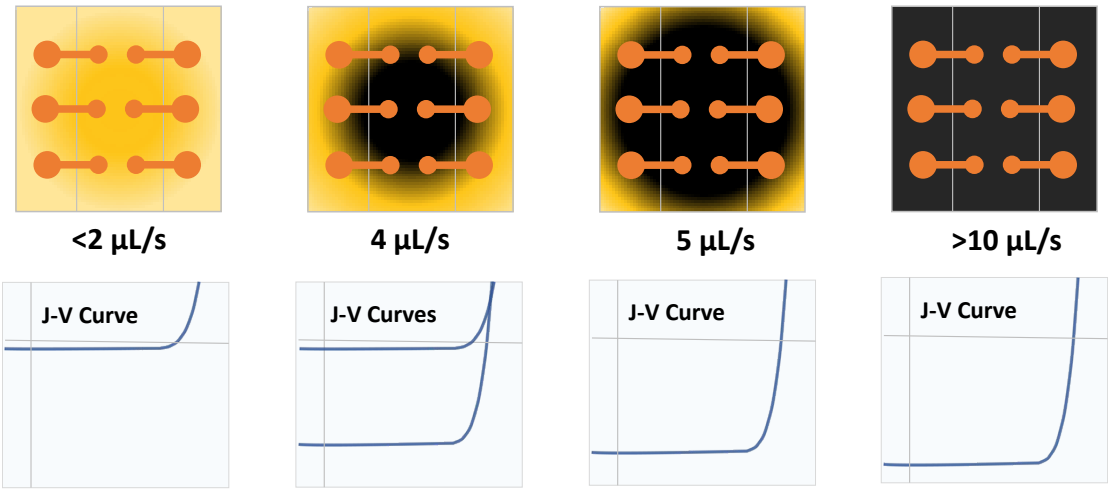

Fig. S14 Schematic diagrams illustrating the surface morphology of the perovskite films formed with different dripping speeds and the corresponding *J-V* curves.

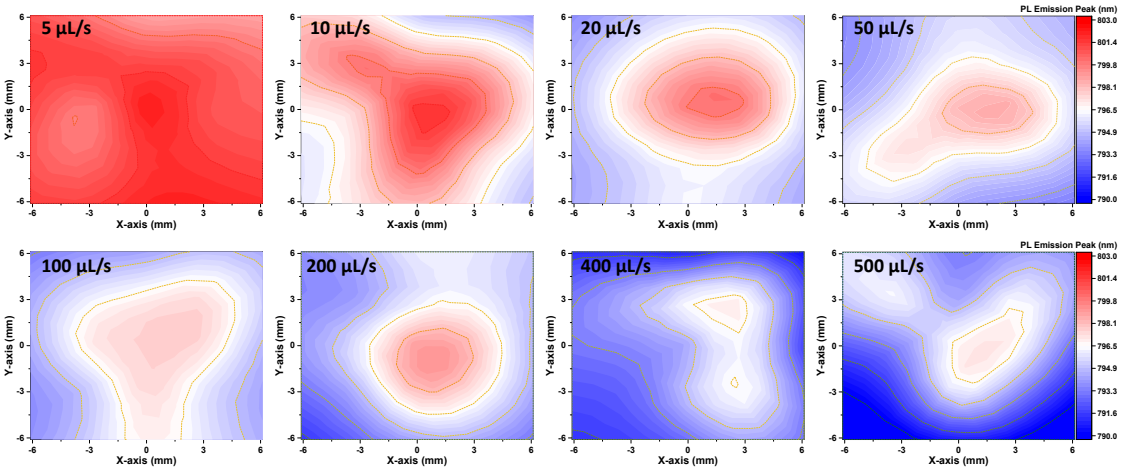

Fig. S15 PL emission peak contour maps for perovskite films prepared with varying dripping speeds of organic ammonium halide. The PL mapping figures are plotted as value maps of slices, with 13 specific points in each film collected.

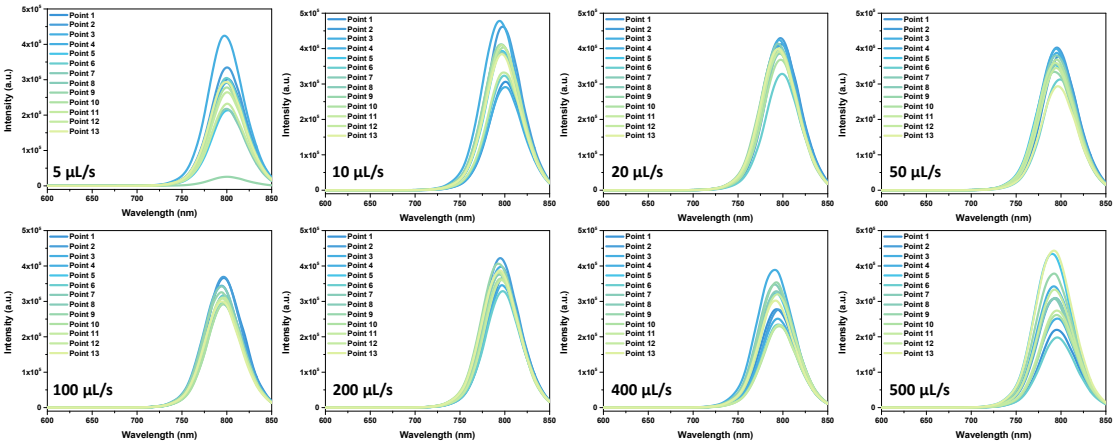

Fig. S16 PL spectra of films fabricated with different dripping speeds. The dripping speeds are 5 to 500 µL/s, respectively. 13 points with regular patterns on each film were measured.

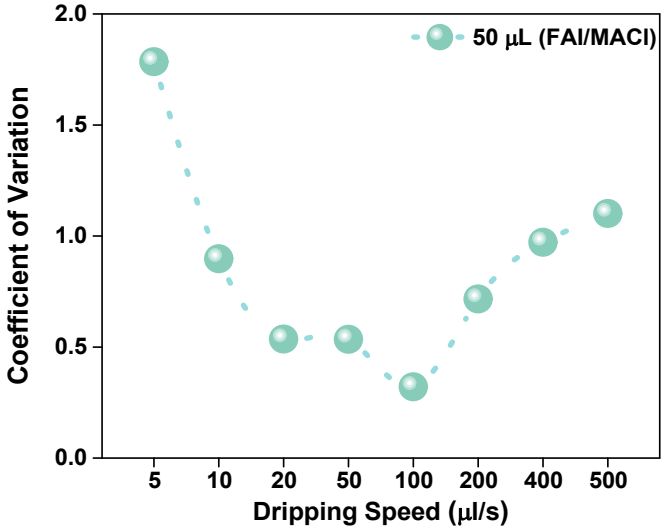

Fig. S17 The CV values of PL peaks intensity for perovskite films with different dripping speeds of ammonium halide solution. The dripping volume of FAI/MACl precursor is 50 μL.

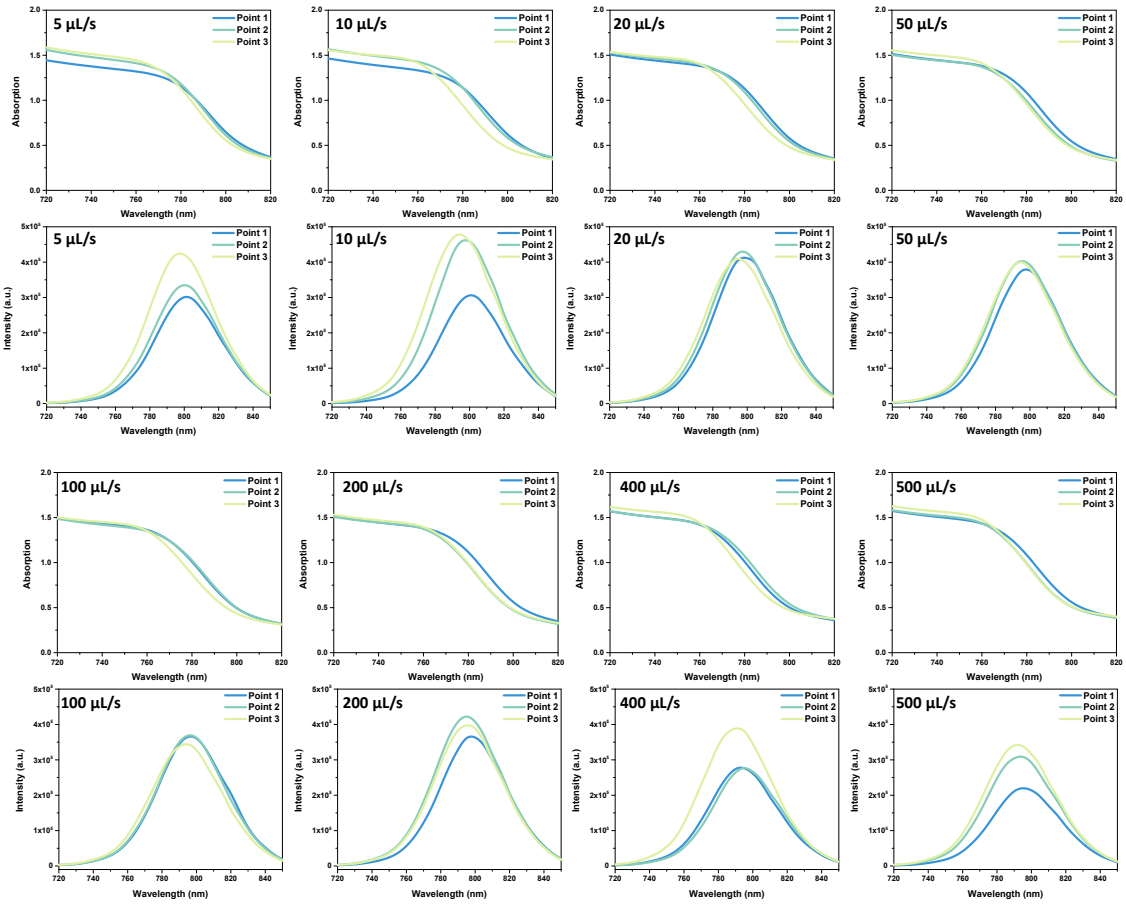

Fig. S18 The UV-Vis absorption and PL spectra for films fabricated with different dripping speeds. Three points on each film were measured and analyzed.

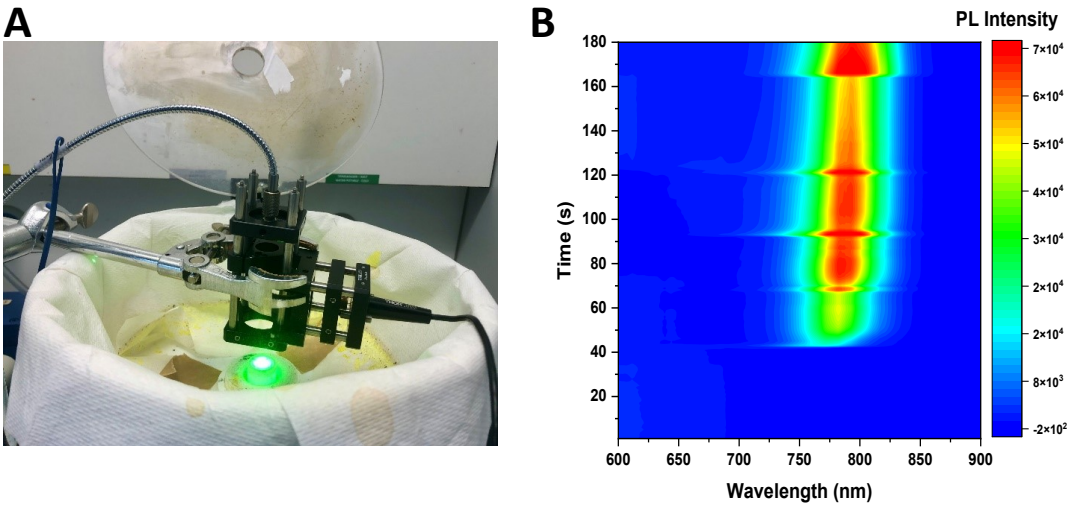

Fig. S19 (A) Photograph of a homemade in-situ PL characterization setup. **(B)** In-situ PL spectra of wet perovskite film fabricated with fast (>50 µL/s) ejection speed but long dripping interval (20-40 s) of FAI/MACl solution. The PL signals were collected during the spin-coating process.

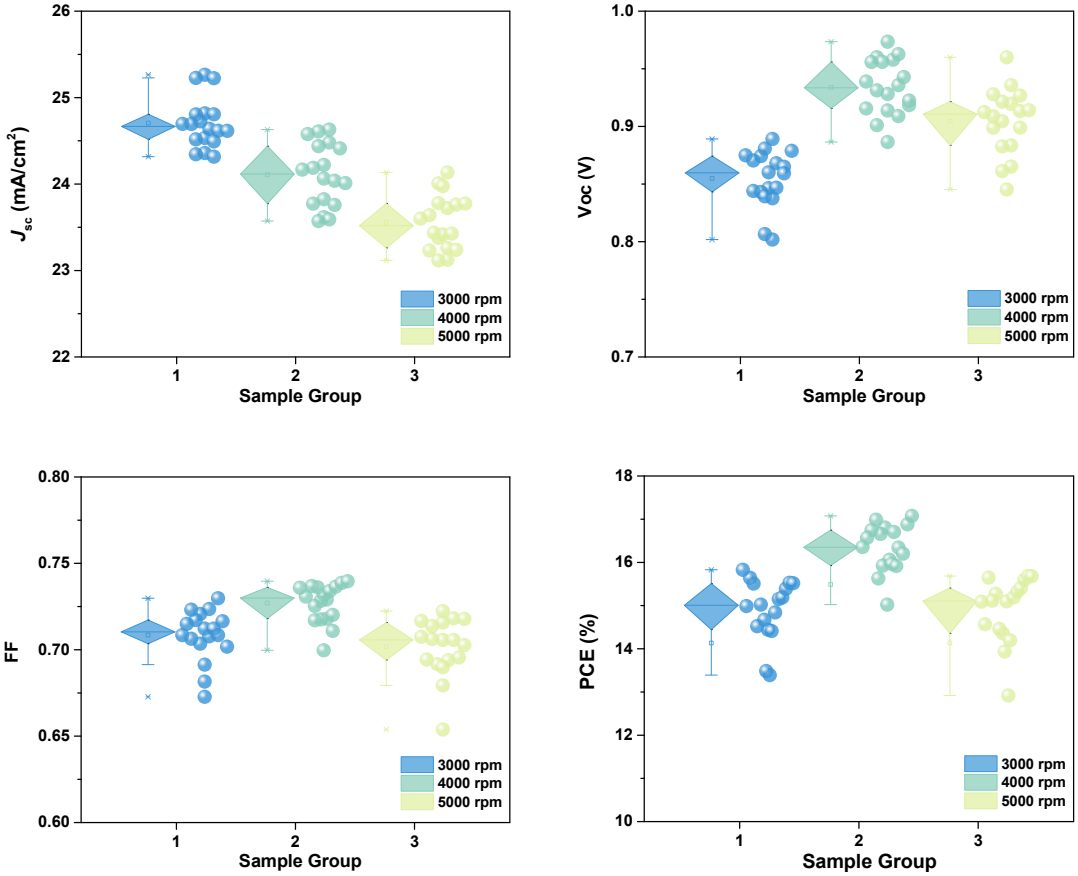

Fig. S20 Performance distribution of perovskite devices fabricated with varying spin speeds (3000, 4000, and 5000 rpm) for the deposition of Spiro-OMeTAD layer. The spin-coating process was performed in a static mode under ambient air conditions.

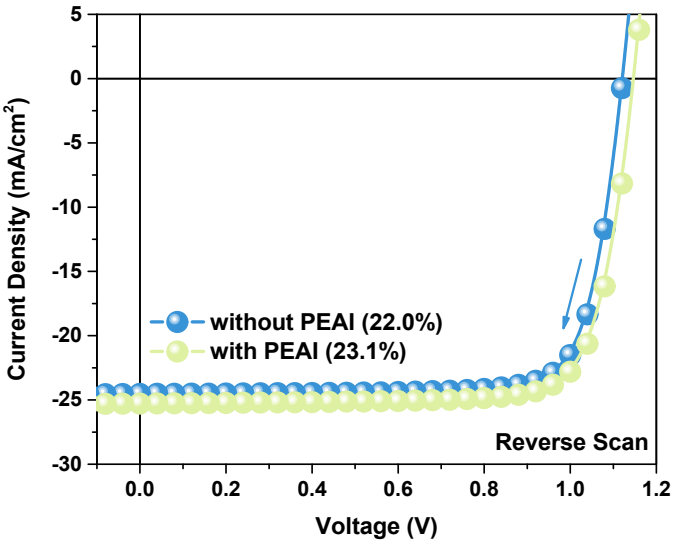

Fig. S21 The *J-V* curves for the champion perovskite devices with and without the PEAI passivation layer.

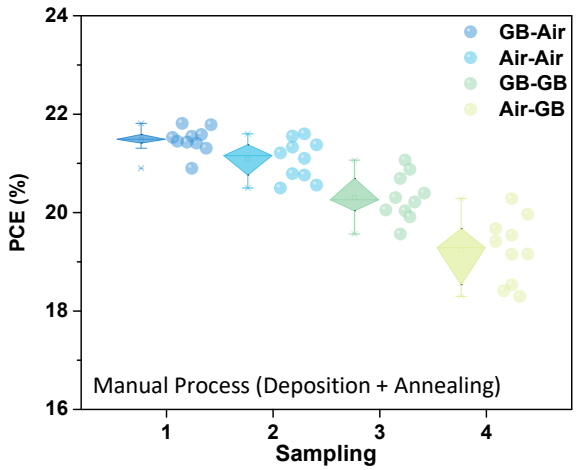

Fig. S22 Performance distribution of best PSCs fabricated in different atmospheres manually. The fabrication process involved thin film deposition (air and glovebox) and post-annealing (air and glovebox) in different atmospheres. The operational room temperature (RT) is 20-25°C and relative humidity (RH) is 30-40%. (Spin speed: 1300 rpm * 1750 rpm)

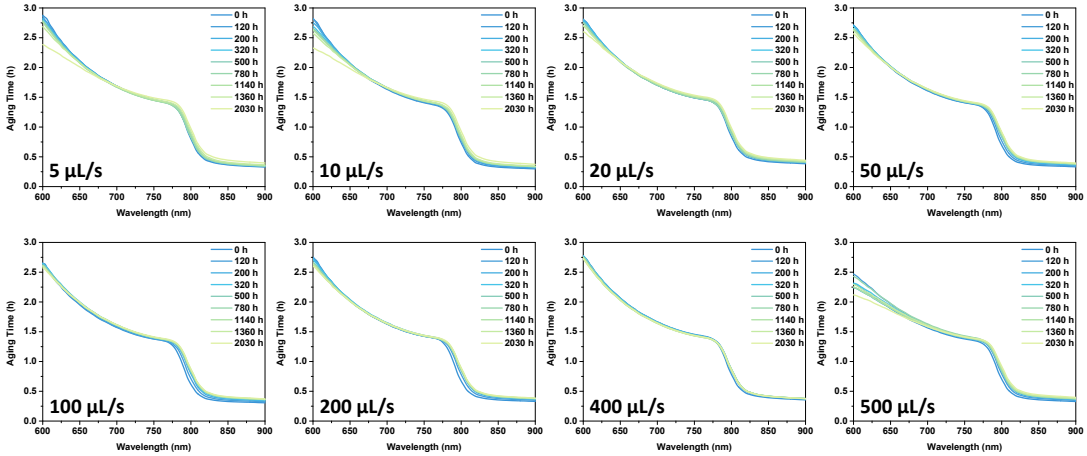

Fig. S23 Evolution of time-dependent absorption of perovskite thin films fabricated with varying drip speeds of organic ammonium halide solution. The unsealed films were aged at 65 °C in a nitrogen-filled chamber under continuous 1-sun metal-halide lamp illumination for 2030 h.

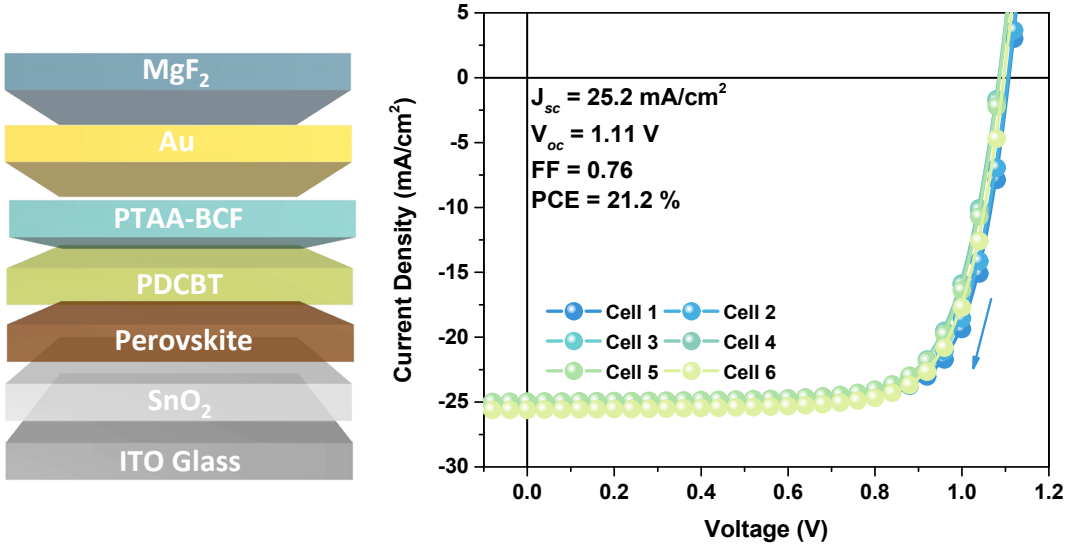

Fig. S24 *J*–*V* curves of the device (ITO/SnO_2/Perovskite/PDCBT/PTAA-BCF/Au/MgF_2) fabricated for photo-thermal stability test.

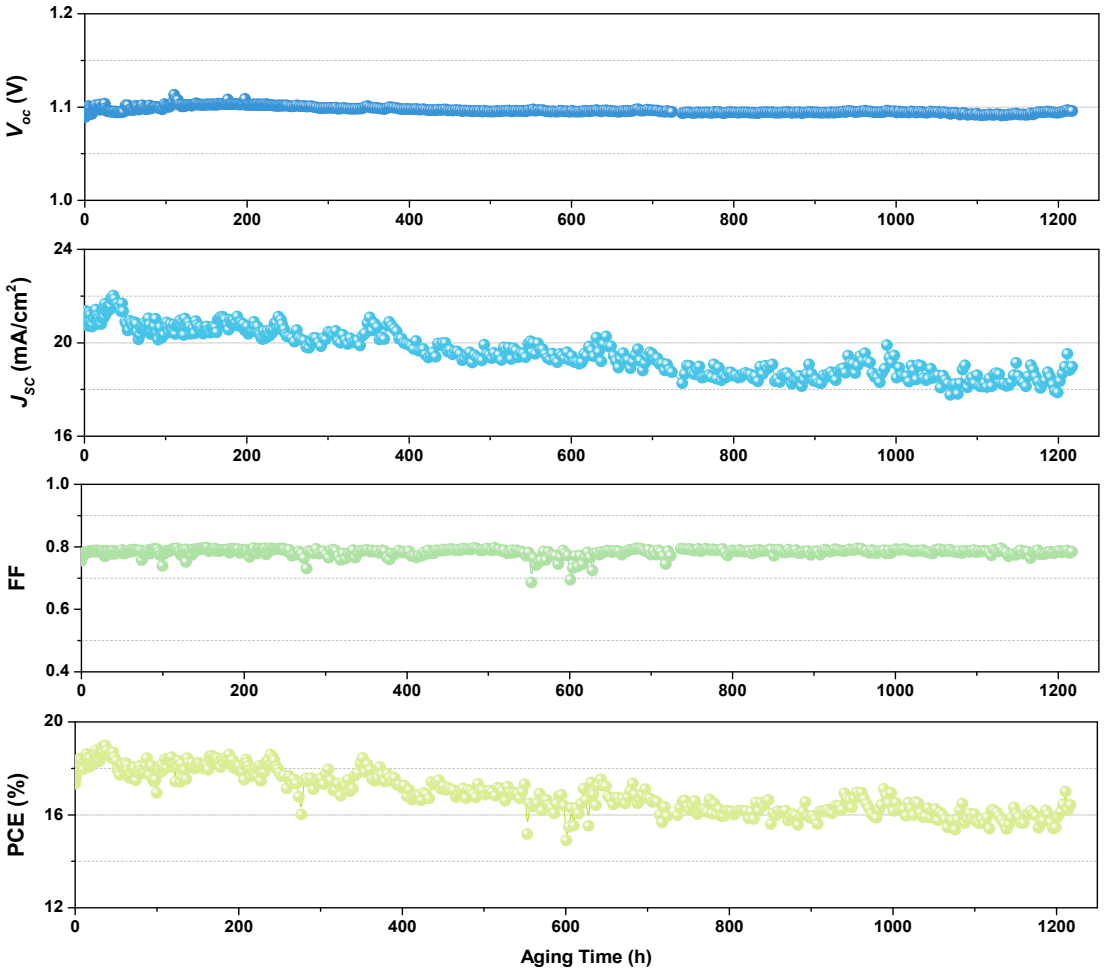

Fig. S25 The results of the long-term stability test. The samples were tested at 60–65°C in a N_2-filled chamber under continuous metal-halide lamp illumination (83 mW/cm^2) in reverse directions.

Table S1 The performance of ambient-processed n-i-p devices prepared with/without additive engineering methods.

Optimization Strategy	Additive	Device Structure	Perovskite Composition	Fabrication Method	PCE	Stability Performance	Year	Ref.
Additive engineering	2-pyridylthiourea	FTO/c-TiO_2/meso-TiO_2/ PVK/Spiro-OMeTAD /Au	$MAPbI_3$	Spin-coating	18.2%	92% after 30 days under air atmosphere	2017	[1]
Additive engineering	methylammonium acetate (MAAc)	ITO/CPTA/BACl/PVK/ Spiro-OMeTAD/MoO_3/Au[1]	$MAPbI_3$	Spin-coating	20.05%	93% after 1000 h under air atmosphere	2019	[2]
Additive engineering	$Pb(SCN)_2$	ITO/SnO_2/PVK/ Spiro-OMeTAD/Au	$MAPbI_3$	Air-blading	20.08%	95% after 700 h of storage in the air	2019	[3]
Additive engineering	NH_4SCN and NH_4Cl	FTO/TiO_2/PVK/ Spiro-OMeTAD/Ag	$MAPbI_{3-x}(SCN)_x$	Spin-coating	16.61%	80% after 30 days in ambient air	2020	[4]
Additive engineering	1,3-bis(4-vinylbenzyl)imidazolium chloride	FTO/c-TiO_2/meso-TiO_2/ PVK/Spiro-OMeTAD/Au	$FA_{0.85}MA_{0.15}PbI_3$ $MAPbI_3$	Spin-coating	19.92% 17%	80% after 4 months of storage in the air 90% after 2000 h of 1-sun illumination	2020	[5]
Additive engineering	MA (ethanol solvent) and MACl	FTO/c-ZnO-ZnS/meso-TiO2/PVK/Spiro-OMeTAD /Au	$MAPbI_3$	Spin-coating	20.3%	/	2020	[6]
Additive engineering	methylammonium thiocyanate	ITO/SnO_2/PVK / spiro-MeOTAD/Au	$FAPbI_3$	Spin-coating	23.1%	90% after 500 h under 1-sun in N_2 atmosphere	2020	[7]
Additive engineering	cellulose acetate (CA)	FTO/TiO_2/PVK/ Spiro-OMeTAD/Ag	$MAPbI_3$	Spin-coating	19.53%	82.60% after placed in 85% relative humidity (RH) for 15 days	2021	[8]
Additive engineering	Ac^- and SCN^- ions	FTO/NiO_x/PVK/Spiro-OMeTAD/Au	$MAPbI_3$	Spin-coating	20.55%	85% after 3600 h of storage in the air	2021	[9]
Additive engineering	Trimethylsulfonium cation (TMS+)	FTO/c-TiO_2/PVK/ Spiro-OMeTAD/Au	$(TMS)_{0.02}(FA)_{0.98}PbI_3$	Spin-coating	17.69%	42% after 130 h of 1-sun illumination, 61.6% after 720 h under air condition	2022	[10]

Additive engineering	Ethylenediammonium iodide ($EDAI_2$)	ITO/PTAA/PVK/ Spiro-OMeTAD/Au	$MAPbI_3$	Spin-coating	20.33%	85 % after 90 days in ambient air	2022	[11]
Additive engineering	n-heptylamine (nHA)	ITO/SnO_2/PVK/ Spiro-OMeTAD/Au	$FAPbI_3$	Spin-coating	23.7%	95% after 1500 h in ambient air	2022	[12]
Additive engineering	PbS quantum dots (QDs)	ITO/SnO_2/PVK/ Spiro-OMeTAD/Au	$FAPbI_3$	Spin-coating	17.08%	80% after 145 days under air atmosphere	2023	[13]
Additive engineering	Formamidine acetate (FAAc)	FTO/TiO_2/PVK/Carbon	$FA_{0.6}MA_{0.4}PbI_3$	Spin-coating	17.69%	92 % after 1000 h of storage in the air	2023	[14]
Additive engineering	potassium thiocyanate (KSCN)	FTO/c-TiO_2/meso-TiO_2/ PVK/Spiro-OMeTAD /Au	$(FA_{0.85}Cs_{0.15})Pb(I_{0.97}Br_{0.03})_3$	Spin-coating	18.1%	82% after 520 h of storage in the air	2023	[15]
Additive engineering	$PbAc_2$ and $PbCl_2$	ITO/SnO_2/PVK/ Spiro-OMeTAD/Au	$MAPbI_3$	Spin-coating	19.91%	100% after 88 days of storage in the air	2023	[16]
Additive engineering	$Pb(SCN)_2$ and PEASCN	FTO/SnO_2/PVK/ Spiro-OMeTAD/Au	$FA_{0.4}MA_{0.6}PbI_3$ $MAPbI_3$	Spin-coating	21% 19.83%	87 % after 21 days in ambient air	2023	[17]
Additive engineering	$Pb(Ac)_2$	ITO/SnO_2/PVK/ Spiro-OMeTAD/Au	$FAPbI_3$	Spin-coating	21.8%	90% after 800 h of light aging test	2023	[18]
Additive engineering	$Mn_3Zn_{1-x}Sn_xN$ compound	FTO/SnO_2/PVK/ Spiro-OMeTAD/Au	$FAMAPbI_3$	Spin-coating	22.4%	93.78% after 90 days in ambient air	2023	[19]
Additive engineering	guanabenz acetate salt	FTO/c-TiO_2/PVK/o-F-PEAI/Spiro-OMeTAD/Au	$MA_{0.02}FA_{0.98}PbI_3$	Spin-coating	25.08%	95% after 500 h under 1-sun in N_2 atmosphere	2023	[20]
Additive engineering	phenolphthalein (PHTH)	ITO/SnO_2/PVK/ Spiro-OMeTAD/Au	$FAPbI_3$	Spin-coating	19.9%	90% after 720 h of storage in the air	2024	[21]
Interface ETL modification	imidazole (ImA) and salicylic acid (SA)	FTO/SnO_2/PVK/ImA/SA Spiro-OMeTAD/Au	$Cs_{0.05}FA_{0.95}PbI_3$	Spin-coating	21.3%	100% after 3380 h of storage in the air environment	2021	[22]
Interface ETL	Sodium of	ITO/S-PASP:SnO_2/PVK/	$Cs_{0.05}(FA_{0.83}MA_{0.17})_{0.95}$	Spin-coating	20.92%	86% after 240 h of 85℃ thermal aging	2023	[23]

modification	Polyaspartic acid	Spiro-OMeTAD/Ag	$Pb(I_{0.83}Br_{0.17})_3$					
Interface ETL modification	Alkali metal salts	FTO/SnO_2-BCA/PVK/PEAI/ Spiro-OMeTAD /Au	$Cs_{0.05}FA_{0.90}MA_{0.05}$ $Pb(I_{0.95}Br_{0.05})_3$	Spin-coating	21.84%	81.2% efficiency after 1200 h under ambient condition	2023	[24]
Interface ETL modification	trisodium citrate (TC)	ITO/TC:SnO_2/PVK/ Spiro-OMeTAD/Au	$Cs_{0.05}FA_{0.85}MA_{0.1}$ $Pb(I_{0.97}Br_{0.03})_3$	Spin-coating	21.17%	81% after 2500 h under air exposure	2024	[25]
Anti-solvent engineering	Mixed dibutyl ether (DB) and diethyl ether (DE)	FTO/AlO_6/SnO_2/PVK/ Spiro-OMeTAD/Au	$Cs_{0.01}FA_{0.94}MA_{0.05}$ $PbI_{2.85}Br_{0.15}$	Spin-coating	22.06%	90% after 1300 h of storage in the air	2021	[26]
Process Optimization	Without additive	FTO/SnO_2/PVK/ Spiro-OMeTAD/Ag	$FA_{0.88}MA_{0.12}Pb$ $I_{2.85}Br_{0.15}$	Drop-casting	21.08%	91.3 % after 80 days in ambient air	2021	[27]
Process optimization	Without additive	ITO/NiO_x/PVK/C60/BCP/Ag (p-i-n structure)	$Cs_{0.17}FA_{0.83}PbI_3$	Rapid spray plasma processing	18.5%	/	2022	[28]
Process optimization	Without additive	ITO/NiO/PVK/PC61BM/BCP/ Al (p-i-n structure)	$MAPbI_3$	Photonic curing	11.42	/	2023	[29]
Process optimization	Without additive	FTO/SnO_2/PVK/Spiro-OMeTAD/Ag	$FAPbI_3$	Spin-coating	20.46%	85% after 1200 h stored under relative humidity levels below 40%	2024	[30]
Process optimization	Without additive	ITO/SnO_2/PVK/PEAI/ spiro-MeOTAD/Au	$MAFAPbI_3$	Spin-coating	23.1%	92% after 1200 h under continuous illumination in N_2-filled chamber at 65℃	2024	This work

Note: [1] CPTA:C60 pyrrolidine tris-acid; BACl: butylamine hydrochloride.

References:

[1] Sun, M., Zhang, F., Liu, H., Li, X., Xiao, Y., & Wang, S. (2017). Tuning the crystal growth of perovskite thin-films by adding the 2-pyridylthiourea additive for highly efficient and stable solar cells prepared in ambient air. *Journal of materials chemistry A*, 5(26), 13448-13456.

[2] Chao, L., Xia, Y., Li, B., Xing, G., Chen, Y., & Huang, W. (2019). Room-temperature molten salt for facile fabrication of efficient and stable perovskite solar cells in ambient air. *Chem*, 5(4), 995-1006.

[3] Ding, J., Han, Q., Ge, Q. Q., Xue, D. J., Ma, J. Y., Zhao, B. Y., ... & Hu, J. S. (2019). Fully air-bladed high-efficiency perovskite photovoltaics. *Joule*, 3(2), 402-416.

[4] Li, Y., Zhang, Z., Zhou, Y., Xie, L., Gao, N., Lu, X., ... & Liu, J. (2020). Enhanced performance and stability of ambient-processed $CH_3NH_3PbI_{3-x}(SCN)_x$ planar perovskite solar cells by introducing ammonium salts. *Applied Surface Science*, 513, 145790.

[5] Xia, R., Gao, X. X., Zhang, Y., Drigo, N., Queloz, V. I., Tirani, F. F., ... & Dyson, P. J. (2020). An efficient approach to fabricate air-stable perovskite solar cells via addition of a self-polymerizing ionic liquid. *Advanced Materials*, 32(40), 2003801.

[6] Huang, X., Chen, R., Deng, G., Han, F., Ruan, P., Cheng, F., ... & Zheng, N. (2020). Methylamine-dimer-induced phase transition toward MAPbI3 films and high-efficiency perovskite solar modules. *Journal of the American Chemical Society*, 142(13), 6149-6157.

[7] Li, R., Ding, J., Mu, X., Kang, Y., Wang, A., Bi, W., ... & Dong, Q. (2022). Hyperbranched phthalocyanine enabling black-phase formamidinium perovskite solar cells processing and operating in humidity open air. *Journal of Energy Chemistry*, 71, 141-149.

[8] Zhang, P., Gu, N., Song, L., Chen, W. H., Du, P., Yin, X., & Xiong, J. (2021). Bifunctional green cellulose derivatives employed for high efficiency and stable perovskite solar cells under ambient environment. *Journal of Alloys and Compounds*, 886, 161247.

[9] Wang, Z., Jin, J., Zheng, Y., Zhang, X., Zhu, Z., Zhou, Y., ... & Tai, Q. (2021). Achieving efficient and stable perovskite solar cells in ambient air through non-halide engineering. *Advanced Energy Materials*, 11(42), 2102169.

[10] Sandhu, S., Rahman, M. M., Senthilkumar, M., Yadagiri, B., Park, J., Yoo, K., & Lee, J. J. (2022). α-FAPbI3 phase stabilization using aprotic trimethylsulfonium cation for efficient perovskite solar cells. *Journal of Power Sources*, 551, 232207.

[11] Chen, H., Yao, G., Yang, S., Liu, X., Cai, M., & Dai, S. (2022). Fabricating stable and efficient perovskite solar cells in air ambient via lattice anchoring strategy. *Chemical Engineering Journal*, 435, 134899.

[12] Wang, M., Sun, H., Meng, L., Wang, M., & Li, L. (2022). A universal strategy of intermolecular exchange to stabilize α-$FAPbI_3$ and manage crystal orientation for high-performance humid-air-processed perovskite solar cells. *Advanced Materials*, 34(23), 2200041.

[13] Salim, K. M., Masi, S., Gualdrón-Reyes, A. F., Sánchez, R. S., Barea, E. M., Krečmarová, M., ... & Mora-Seró, I. (2021). Boosting long-term stability of pure formamidinium perovskite solar cells by ambient air additive assisted fabrication. *ACS Energy Letters*, 6(10), 3511-3521.

[14] Li, L., Zhang, R., Wu, Z., Wang, Y., Hong, J., Rao, H., ... & Zhong, X. (2023). Crystallization control of air-processed wide-bandgap perovskite for carbon-based perovskite solar cells with 17.69% efficiency. *Chemical Engineering Journal*, 455, 140566.

[15] Bensekhria, A., Asuo, I. M., Ka, I., Nechache, R., & Rosei, F. (2023). Improved Performance of Air-Processed Perovskite Solar Cells via the Combination of Chlorine Precursors and Potassium Thiocyanate. *ACS Applied Materials & Interfaces*, 15(48), 56413-56423.

[16] Ahmed, Y., Thrithamarassery Gangadharan, D., Kokaba, M. R., Yeddu, V., Awais, M., Zhang, D., ... & Saidaminov, M. I. (2023). All-Scalable $CH_3NH_3PbI_3$ Perovskite Solar Cells Fabricated in Ambient Air. *Solar RRL*, 7(15), 2300288.

[17] Zhu, Z., Shang, J., Tang, G., Wang, Z., Cui, X., Jin, J., ... & Tai, Q. (2023). Vertical distribution of PbI_2 nanosheets for robust air-processed perovskite solar cells. *Chemical Engineering Journal*, 454, 140163.

[18] Chen, L., Liu, T., Yu, H., Zhang, Z., Qin, C., Zhang, N., ... & Liu, Z. (2023). Modulated crystallization and enhanced stable of high efficient perovskite solar cells with $Pb(Ac)_2$. *Journal of Alloys and Compounds*, 942, 168924.

[19] Zhang, W., He, L., Zhou, Y., Tang, D., Ding, B., Zhou, C., ... & Li, X. (2023). Multiple roles of negative thermal expansion material for high-performance fully-air processed perovskite solar cells. *Chemical Engineering Journal*, 457, 141216.

[20] Yan, L., Huang, H., Cui, P., Du, S., Lan, Z., Yang, Y., ... & Li, M. (2023). Fabrication of perovskite solar cells in ambient air by blocking perovskite hydration with guanabenz acetate salt. *Nature Energy*, 8(10), 1158-1167.

[21] Elbohy, H., Suzuki, H., Nishikawa, T., Kyaw, A. K. K., & Hayashi, Y. (2024). Phenolphthalein: A Potent Small-Molecule Additive for High-Performance and Ambient-Air-Stable $FAPbI_3$ Perovskite Solar Cells. *ACS Applied Energy Materials*, 7(7), 2925–2937.

[22] Salim, K. M., Masi, S., Gualdrón-Reyes, A. F., Sánchez, R. S., Barea, E. M., Kreĉmarová, M., ... & Mora-Seró, I. (2021). Boosting long-term stability of pure formamidinium perovskite solar cells by ambient air additive assisted fabrication. *ACS Energy Letters*, 6(10), 3511-3521.

[23] Chen, L., Liu, Z., Qiu, L., Xiong, J., Song, L., & Du, P. (2023). Multifunctional Regulation of SnO_2 Nanocrystals by Snail Mucus for Preparation of Rigid or Flexible Perovskite Solar Cells in Air. *ACS nano*, *17*(23), 23794-23804.

[24] Ning, L., Zha, L., Duan, R., Gu, N., Du, P., Song, L., ... & Xiong, J. (2023). Fabrication of perovskite solar cells with PCE of 21.84% in open air by bottom-up defect passivation and stress releasement. *Chemical Engineering Journal*, *471*, 144279.

[25] Liu, G., Zeng, G., Ren, Z., Liu, J. and Li, X. (2024), Enhancing Interface Interaction through Multifunctional Trisodium Citrate Modification of Electron-Transport Layer in Fully Air-Processed Perovskite Solar Cells. *Sol. RRL*, 8: 2400043. https://doi.org/10.1002/solr.202400043

[26] Jung, K., Oh, K., Choi, J. W., Kim, K. C., & Lee, M. J. (2021). Ambient-air fabrication of stable mixed cation perovskite planar solar cells with efficiencies exceeding 22% using a synergistic mixed antisolvent with complementary properties. *Nano Energy*, 89, 106387.

[27] Liu, L., Zuo, C., & Ding, L. (2021). Self-spreading produces highly efficient perovskite solar cells. *Nano Energy,* 90, 106509.

[28] Liu, Z., Rolston, N., Flick, A. C., Colburn, T. W., Ren, Z., Dauskardt, R. H., & Buonassisi, T. (2022). Machine learning with knowledge constraints for process optimization of open-air perovskite solar cell manufacturing. *Joule*, 6(4), 834-849.

[29] Xu, W., Liu, Z., Piper, R. T., & Hsu, J. W. (2023). Bayesian Optimization of photonic curing process for flexible perovskite photovoltaic devices. *Solar Energy Materials and Solar Cells*, 249, 112055.

[30] Porwal, S., Bansal, N. K., Ghosh, S., & Singh, T. (2024). Stress-induced stabilization of the photoactive $FAPbI_3$ phase under ambient conditions without using an additive

approach. *Energy Advances*. 3, 894-903